

*Journal of*  
***Mechanics of***  
***Materials and Structures***

**EFFECTIVE PROPERTIES OF SHEAR BAND STRUCTURES IN  
ROCK  
AT DIFFERENT LENGTH SCALES**

John Napier

***Volume 3, N° 5***

***May 2008***



## EFFECTIVE PROPERTIES OF SHEAR BAND STRUCTURES IN ROCK AT DIFFERENT LENGTH SCALES

JOHN NAPIER

Failure localization in rock is observed ubiquitously on geological scales in the form of fault or earthquake damage structures. Similar failure processes are observed in confined compression tests carried out on laboratory-scale rock samples. At an intermediate scale, seismic activity is often associated with the formation of so-called burst fractures that are intermittently formed and exposed in the vicinity of deep level mining operations. Computational modeling can assist the understanding of the complex nature of these failure processes. The present study investigates the question of how the properties of macroscopic shear band features are controlled by microscopic constitutive behavior. The computational approach that is used is to consider the formation of shear band structures by selectively mobilizing members of an assembly of randomly oriented cracks that are modeled as displacement discontinuity elements. Particular issues that are addressed are the question of whether the microscopic failure processes are self-similar to the macroscopic processes, and how the density of the discontinuity assembly affects the localization patterning. It appears that the use of slip or tension-weakening constitutive models yields equivalent “macro” results that are independent of the “micro” mesh density for a given mesh type. If the intrinsic junction coordination of the mesh is altered, it is found that the equivalent macro dilation angle is changed. This has important implications in determining whether a particular distinct element or lattice model with an intrinsic junction structure is capable of replicating the observed failure behavior of a given rock type. A dimensionless parameter group is suggested as a measure of the intrinsic coordination number for a random crack model of rock micro structure.

### 1. Introduction

Computational modeling of rock failure processes is of great practical value in determining the onset and consequences of stress changes induced by earthquakes, by mining operations, and by the construction of large structures such as dams. This requires the quantitative evaluation of the interactive nature of tectonic loading and of excavation or construction steps and the attendant mobilization of discontinuities and possible fracture of intact rock. A comprehensive review of numerical modeling procedures has been compiled by Jing [2003]. However, the formulation of appropriate constitutive models to use in numerical simulations of rock failure processes is very difficult. Consequently, many computational schemes have been designed to solve discrete assemblies of interacting blocks, bonded particles, or other simple lattice structures that can be assembled to represent macroscopically complex failure patterns. The pioneering development of the so-called Distinct Element Method (DEM) [Cundall 1988; Hart et al. 1988; Potyondy and Cundall 2004] is of particular interest. Numerous applications of distinct element and other lattice models have been applied towards the simulation of granular and quasibrittle material failure in rock, concrete structures, and large-scale fault systems. Representative examples of

---

*Keywords:* fracturing, numerical modeling, shear bands.

these applications are reported in [Lockner and Madden 1991a; 1991b; Bolander et al. 1996; Chiaia et al. 1997; Morgan and Boettcher 1999; Morgan 1999; Budhu et al. 1999; Jefferson et al. 2002; Kuhn 2005; Rechenmacher 2006]. In these examples, failure is initiated by selected breakage or slippage of bonds or linkages within a simulated lattice structure or particle assembly. Individual bonds, interfaces, and internal linkages are assigned simple failure rules and the entire system is allowed to evolve under selected loading steps. Consequent micro fracture sequences are tracked during the simulation and macro coalescence and localization mechanisms are noted. The approach can be applied as well to the study of rock fracture by selecting crack elements sequentially from a random assembly of potential crack positions and evaluating the stress and displacement movements induced by the mobilized cracks using the displacement discontinuity boundary element method; see, for example, [Napier and Peirce 1995; Napier and Malan 1997; Sellers and Napier 1997].

It is apparent that the distinct element and other lattice models are very fruitful in gaining some appreciation of the complex fracture patterning and sequencing that may arise from the incremental loading or straining of particular problem configurations. A number of troublesome issues, though, are not addressed generally. These include the following basic questions:

- Does the characteristic size of the underlying lattice element (for example, particle size, block size, crack length, spring element) affect the emergent failure pattern?
- How should the intrinsic failure rules that are assigned to the micro structure components be assigned or calibrated?
- Do these micro structures have to bear a direct relationship to the actual material micro properties (for example, pore sizes, micro cracks, grain boundaries) and at what length scale should this correspondence be established?
- Can macro failure mechanisms, such as shear bands, be represented by appropriate macro geometric objects, such as individual slip lines, and can the equivalent constitutive properties of the macro objects be deduced from the assigned micro element properties?
- How many micro-macro hierarchical scales should be considered in modeling the material behavior at a given scale of interest?

This paper attempts to address some of these questions by considering a random fracture network simulation of shear failure through an intact bridge region between two adjacent sliding discontinuities. The problem is restricted initially to plane strain conditions. Micro-level failure is assumed to be initiated from a random assembly of crack elements that are at least an order of magnitude smaller than the bridge width. The resulting failure mechanism is then compared to the simulation of the rock bridge as an equivalent slip line linking the adjacent sliding discontinuities. An important property of the fine-scale micro system is identified which appears to control the effective behavior of the macro slip line. This property is related to the connectivity of the random mesh structure at each mesh junction point in terms of the number of potential mesh segments that are attached to each junction and can be thought of as a junction coordination number. It is demonstrated that this topological property of the mesh controls the macro strain behavior of the equivalent slip line failure mechanism and may, in general, determine whether any particular lattice model is intrinsically suitable to simulate failure in a given bonded/disordered material such as rock.

## 2. Rock failure simulation model

The displacement discontinuity boundary element method (see, for example, [Crouch and Starfield 1983]) is used in the present study to formulate a lattice-type failure model comprising multiple interacting crack segments. It is assumed that loading rates are sufficiently slow that inertial (wave propagation) effects can be neglected. Similar results can, in principle, be obtained by using any computational framework that can represent the interaction of multiple intersecting crack discontinuities in a continuous elastic host medium. Suitable numerical models would include the Distinct Element approach of Cundall [1988], and Finite Element codes having appropriate joint element features (see also [Jing 2003]). The displacement discontinuity boundary element method (DDBEM) does offer a number of useful advantages in terms of computational efficiency when the problem can be considered to comprise multiple crack structures that are embedded within an “infinite” region as only the significant crack surfaces are modeled. The main disadvantages of the DDBEM approach are the necessary assumptions of a fundamental influence function solution for the host medium. These issues are of secondary importance in the context of the present study. Some selected examples of the application of the DDBEM to the study of fracture interaction and propagation processes are reported by [Scavia 1992; Napier and Hildyard 1992; Bobet and Einstein 1998] and [Allodi et al. 2003].

A series of numerical experiments were performed to simulate shear-driven failure between two pre-existing sliding discontinuities labeled  $AB$  and  $CD$  respectively as shown in Figure 1. The dimension,  $R$ , of the rock bridge between points  $B$  and  $C$  in Figure 1 is set to 10 units of length, and the sliding discontinuities are each 50 units in length. These units may be considered nominally to be millimeters although the length scale is actually implied by the ratio of the material shear modulus to the slip-weakening parameter used in the failure model that is described later. A random mesh of potential micro crack segments is superimposed on the rectangular region covering the inner tips of the sliding discontinuities as depicted in Figure 1. Remote compressive principal stress loading components  $P_1$  and  $P_2$  are applied at an oblique angle of 22.5 degrees to the pre-existing discontinuities to induce sliding movements and consequent fracturing in the random mesh region. In the present case,  $P_1$  is increased in a series of 24 incremental steps from 20 MPa to 135 MPa, and  $P_2$  is held fixed at a value of 5 MPa. Within

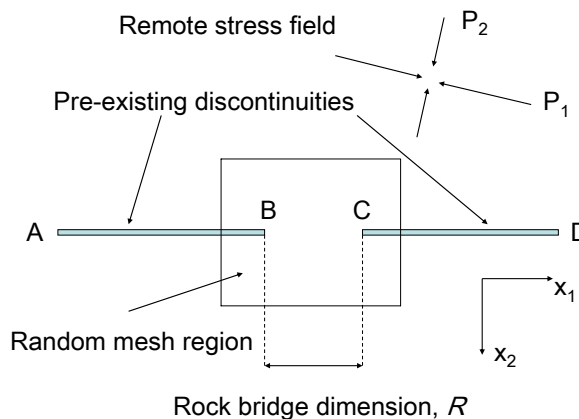


**Figure 1.** Geometry, principal loading, and dimensions for the numerical experiments.

each load increment, fractures are activated in sequence from the random mesh region according to a defined failure priority. Each activated crack element is assumed to be a straight line segment. The shear slip and crack opening displacement discontinuity components can be defined with respect to a local  $x$ - $y$  coordinate system that is centered on each crack element. Suppose that a particular crack element falls in the region  $-b \leq x \leq b$  on the  $x$ -axis. Define the shear and normal components of the displacement discontinuity vector at the point  $x = \eta$  to be  $D_x(\eta)$  and  $D_y(\eta)$ , respectively, where, for each component  $k$ ,

$$D_k(\eta) = u_k^+(\eta) - u_k^-(\eta) \tag{1}$$

represents the difference in the displacement vector components between the positive (+) and negative (-) sides of the crack with respect to the direction of the positive normal to the crack line.

Define the complex valued discontinuity vector  $\Delta(\eta) = D_x(\eta) + iD_y(\eta)$ , where  $i = \sqrt{-1}$ . It can then be shown (see, for example, [Linkov and Mogilevskaya 1994; Mogilevskaya 2000]) that the induced in-plane stress tensor components  $\sigma_{xx}$ ,  $\sigma_{xy}$ , and  $\sigma_{yy}$ , are given by the integral relationships

$$\sigma_{xx} + \sigma_{yy} = \frac{iG}{2\pi(1-\nu)} \int_{-b}^b \left\{ \frac{\bar{\Delta}(\eta)}{(\bar{Z} - \eta)^2} - \frac{\Delta(\eta)}{(Z - \eta)^2} \right\} d\eta, \tag{2}$$

$$\sigma_{yy} - \sigma_{xx} + 2i\sigma_{xy} = \frac{iG}{2\pi(1-\nu)} \int_{-b}^b \left\{ \frac{(\bar{\Delta}(\eta) - \Delta(\eta))}{(Z - \eta)^2} + \frac{2(\bar{Z} - \eta)}{(Z - \eta)^3} \right\} d\eta, \tag{3}$$

where  $G$  is the shear modulus,  $\nu$  is Poisson's ratio, and  $Z = x + iy$  is the field point at which the stress components are evaluated. (Note also that the following relationships hold:  $\bar{\Delta} = D_x - iD_y$  and  $\bar{Z} = x - iy$ ). In the present study, it is assumed that each of the displacement discontinuity components  $D_k(\eta)$ , for  $k = x$  or  $y$ , has a linear variation along the element of the form

$$D_k(\eta) = p_k + q_k\eta, \tag{4}$$

where  $p_k$  and  $q_k$  are constants that are chosen to ensure that the stress tensor components satisfy local equilibrium boundary conditions at two collocation points located within each element. In this case, the integral expressions in Equations (2) and (3) can be determined from the evaluation of simple integrals of the form

$$I_j(Z) = \int_{-b}^b \frac{\eta^j d\eta}{(Z - \eta)}, \quad j = 0 \text{ and } 1 \tag{5}$$

and

$$I_0(Z) = \ln \left[ \frac{Z + b}{Z - b} \right], \quad I_1(Z) = Z I_0(Z) - 2b. \tag{6}$$

Additional expressions can be derived for higher order variation displacement discontinuity vector distributions and for special crack tip shapes, but these possibilities are not considered in the present study.

Each fracture simulation experiment is carried out in a series of incremental crack growth cycles. During each cycle the normal and shear stress traction vector components are evaluated at each collocation point of the current population of unmobilized crack elements that exist in the set of defined mesh segment positions. The normal and shear traction components are determined with respect to the local tangent and normal directions of each mesh segment. A choice is then made of the most likely element to fail according to the effective distance (in terms of the normal and shear traction components) from

a specified failure envelope. Once this choice has been made, the element is added to the population of active crack elements and the entire problem is solved again. The search procedure is continued until no additional crack elements are mobilized. The entire cycle is then repeated for the specified number of far field incremental loading steps. Further details of this approach have been reported in [Napier and Malan 1997].

Figure 2 illustrates the explicit form of the failure envelope and the definition of the stress distance in terms of the normal component  $\sigma_n$  and shear stress component  $\tau$  acting at a point on a given crack segment. When the normal stress component is tensile (as in the case of point *A* in Figure 2), the failure envelope is assumed to follow a power law of the form

$$|\tau| = S_0(1 - \sigma_n/T_0)^\gamma, \quad (7)$$

where  $S_0$  is the intact cohesive strength and  $T_0$  is the intact tensile strength of the material at the collocation point.  $\gamma$  is a dimensionless exponent such that  $0 < \gamma \leq 1$ . The functional form of Equation (7) is chosen to ensure that the failure envelope is smooth in the tensile region and avoids the introduction of a corner point corresponding to a simple tension cut-off parameter. The distance from point *A* to the failure envelope is measured in the direction of the local origin as depicted in Figure 2. When the normal stress component is compressive ( $\sigma_n < 0$ ), as for point *B* in Figure 2, the failure envelope is assumed to follow a linear Mohr–Coulomb relationship of the form

$$|\tau| = S_0 - \mu_0\sigma_n, \quad (8)$$

where  $\mu_0$  is the intact internal coefficient of friction of the material. The distance from point *B* to the failure envelope is assumed to be the vertical distance, parallel to the shear stress axis, as shown in Figure 2.

Once failure is initiated, the cohesive strength and tensile strength are assumed to reduce to zero as linear functions of the slip and crack opening displacements,  $D_x$  and  $D_y$ , respectively. The explicit

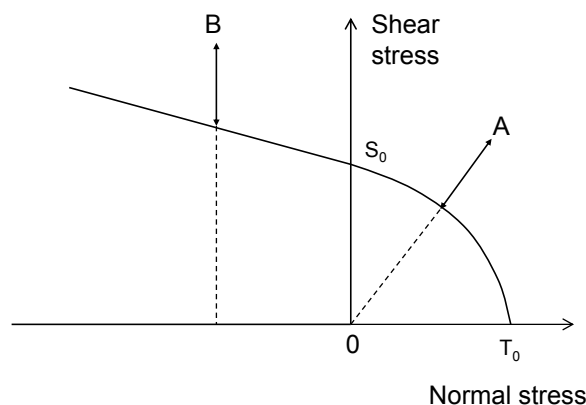


**Figure 2.** Schematic depiction of the assumed composite failure envelope and definition of the distance of a point from the envelope in terms of normal and absolute shear stress coordinates with respect to a local discontinuity segment line (the normal stress is assumed to be positive when it is tensile).

relationships that are assumed are of the form

$$S = S_0 - \alpha |D_x|, \quad (9)$$

$$T = T_0 - \beta D_y, \quad (10)$$

where  $S$  and  $T$  are the current values of the shear strength and the cohesion, and  $\alpha$  and  $\beta$  are the shear and tension weakening parameters, respectively. The values of  $S$  and  $T$  are set to zero when the maximum slip and opening displacements implied by Equations (9) and (10) are exceeded. The composite failure envelope, shown in Figure 2, is updated progressively as failure continues by substituting the current values of  $S$  and  $T$  for  $S_0$  and  $T_0$  in Equations (7) and (8), respectively. It is further assumed that the progressive change in the failure envelope is such that  $S$  and  $T$  both reach zero simultaneously, and that the friction coefficient  $\mu$  changes congruently from the intact value  $\mu_0$  to a specified residual value  $\mu_f$  as these changes proceed. The failure envelopes in the tensile and compressive regions in Figure 2 are assumed to have the same slope when  $\sigma_n = 0$ . This, in turn, implies that the exponent  $\gamma$  must satisfy the relationship

$$\gamma = \mu T/S. \quad (11)$$

The slip-weakening concept [Palmer and Rice 1973; Uenishi and Rice 2003] has a number of important implications. In particular, the weakening behavior imposes an implicit length scale on the material (in some sense analogous to the mean particle size of a particle model) and also implies that numerical experiments of self-similar geometric configurations will exhibit size effects. In addition, it is important to note that the ratio of the host material shear modulus  $G$  to the shear weakening parameter  $\alpha$  is proportional to an implicit slip nucleation length  $h_n$  for a single discontinuity [Uenishi and Rice 2003].

### 3. Effect of random mesh density

A series of three numerical experiments were performed to assess the consequences of changing the density of the random mesh in the rectangular failure region shown in Figure 1. Specific material strength parameters and slip and tension weakening parameters used in the numerical experiments are summarized in Table 1. These parameters were chosen to be appropriate for a failure region having a characteristic size that is nominally of the order of 10 millimeters. The length scale  $\bar{g}$  of the micro flaws comprising the random mesh structure is assumed to be at least one order of magnitude smaller than the bridge dimension  $R$  between points  $B$  and  $C$  in Figure 1 (that is,  $\bar{g} \leq 1$  mm). The mesh segment sizes were consequently also much smaller than the slip nucleation length,  $h_n \sim G/\alpha = 6$  mm, implied by the parameters given in Table 1. The relative areas under the cohesion and tension weakening curves can be inferred from the parameters in Table 1 to have a ratio of about 15:1. This ratio can be considered, as well, to reflect the ratio of the intrinsic specific fracture energy required to mobilize shear micro cracks compared to the energy required to mobilize tensile micro cracks with an equivalent area.

Three different Delaunay mesh tessellations (designated as  $A$ ,  $B$ , and  $C$ ) were considered to determine the effect of the mesh density on the evolution of inelastic strain components in the rock bridge region. The size-frequency distribution of the mesh segments corresponding to each applied tessellation pattern is plotted in Figure 3. An approximate mesh density parameter,  $\rho$ , can be defined to be

$$\rho = L/\sqrt{A_T}, \quad (12)$$

Shear modulus	30000 MPa
Poisson's ratio	0.2
Cohesion, $S_0$	20.0 MPa
Tensile strength, $T_0$	8 MPa
Internal friction coefficient, $\mu_0$	1.0
Residual friction coefficient, $\mu_f$	0.577
Cohesion weakening slope, $\alpha$	5000 MPa/mm
Tensile strength weakening slope, $\beta$	8000 MPa/mm

**Table 1.** Summary of material properties used in numerical experiments of shear fracture.

where  $L$  is the total length of all segments in the tessellation region, and  $A_T$  is the area of this region. The values of  $\rho$  corresponding to each mesh are included in Figure 3. The mean segment lengths,  $\bar{g}$ , for the cases  $A$ ,  $B$ , and  $C$  are, respectively, equal to 1.023 mm, 0.525 mm, and 0.254 mm (see also, Table 3). Note that the coarsest mesh size,  $\bar{g}_A = 1.023$  mm, for mesh  $A$  is chosen to be small relative to both the rock bridge dimension,  $R$ , and the slip nucleation length,  $h_n$ . (Specifically,  $\bar{g}_A/R \sim 0.1$  and  $\bar{g}_A/h_n \sim 0.17$ ). The finer mesh sizes for cases  $B$  and  $C$  were chosen to be approximately equal to one half and one quarter of the initial mesh, respectively, but no special significance is associated with these ratios. Figure 4 shows plots (with displacements magnified by a factor 10) of the fracture patterns developed in the rock bridge region after 24 load step increments of the far-field principal stress component  $P_1$ , for each mesh  $A$ ,  $B$ , and  $C$ . The crack segments that are initiated in shear mode (that is, when the normal stress values in Figure 2 are negative) are depicted as thick (green) lines in contrast to the crack segments that are initiated under tension conditions (thin lines). It is apparent that both tension and shear failure

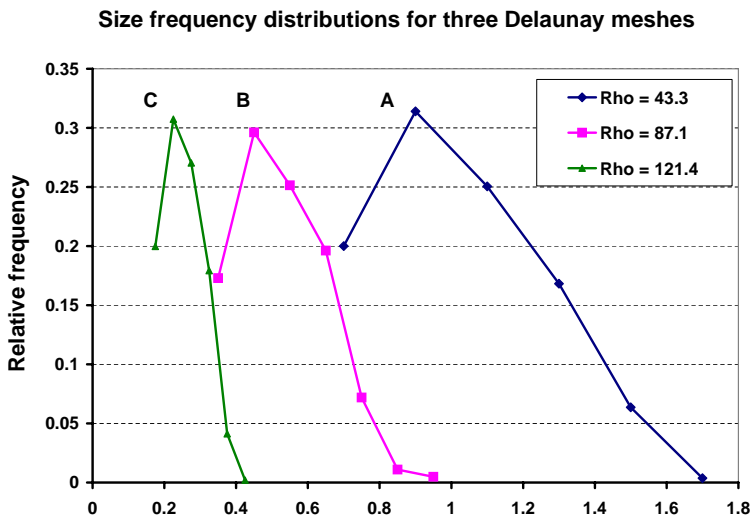


**Figure 3.** Size-frequency distributions of three Delaunay mesh grids used to simulate failure in the rock bridge region shown in Figure 1.

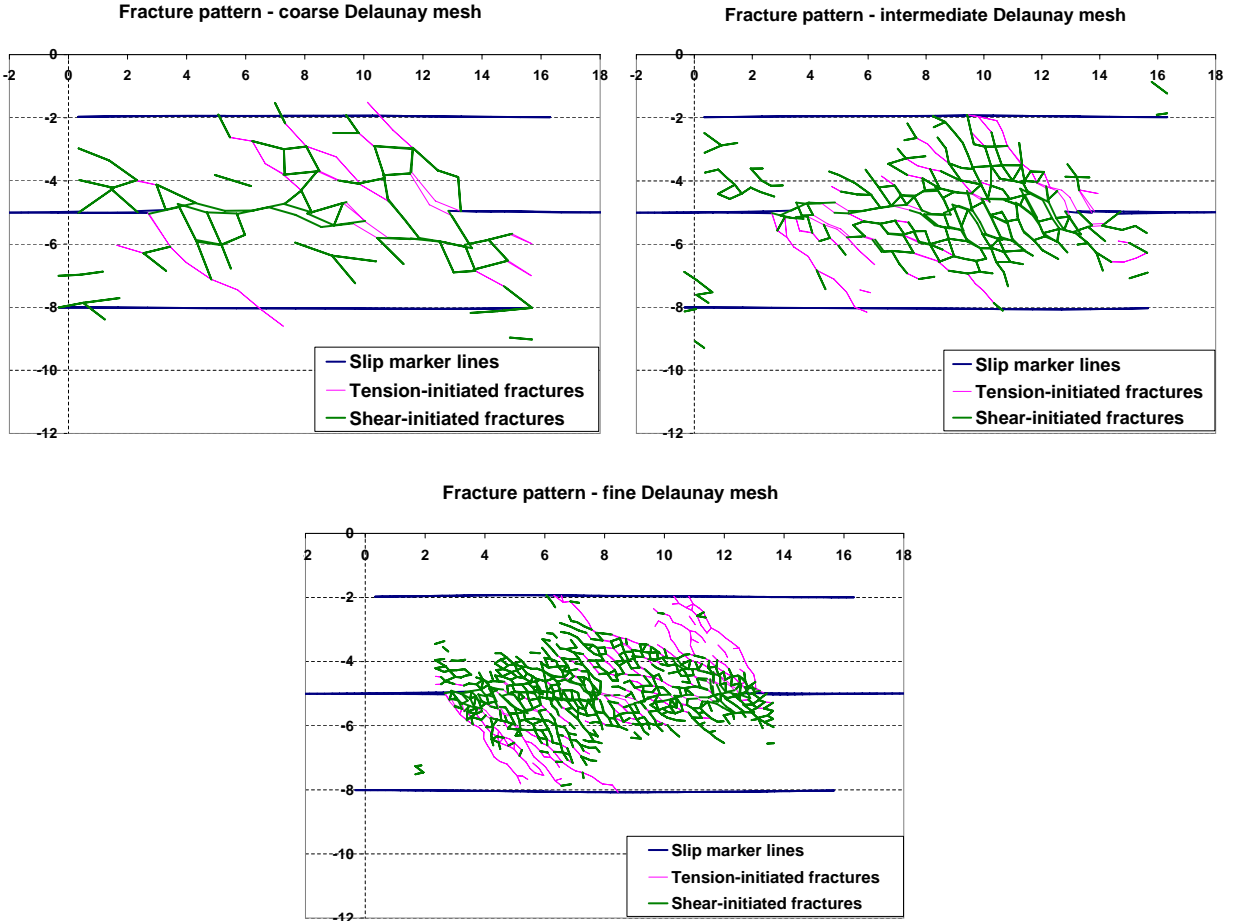


**Figure 4.** Fracture patterns developed for each Delaunay mesh after 24 load step increments: Coarse (top left), intermediate (top right), and fine (bottom) mesh density.

modes are important in establishing the overall fracture patterns shown in Figure 4. It is apparent as well that the total length of activated crack segments increases as the mesh density increases.

The average strain components,  $\bar{\epsilon}_{ij}$ , within the rock bridge region (expressed in the global  $x_1$ - $x_2$  coordinate system shown in Figure 1), are computed for each mesh simulation using the following sum that is taken over all the elements,  $k$ , in the region with a total area  $A_T$ .

$$\bar{\epsilon}_{ij} = \frac{1}{2A_T} \sum_k (\bar{D}_i^{(k)} n_j^{(k)} + \bar{D}_j^{(k)} n_i^{(k)}) g_k. \tag{13}$$

In Equation (13),  $\bar{D}_i^{(k)}$  is the average value of component  $i$  of the discontinuity vector for element  $k$ ,  $n_i^{(k)}$  is the value of component  $i$  of the normal vector to element  $k$ , and  $g_k$  is the length of element  $k$ . The discontinuity and normal vector components are expressed in the global  $x_1$ - $x_2$  coordinate system. The average strain components  $\bar{\epsilon}_{11}$ ,  $\bar{\epsilon}_{12}$ , and  $\bar{\epsilon}_{22}$  are plotted in Figure 5 for each mesh density. The nominal mesh segment sizes of 1 mm, 0.5 mm and 0.25 mm, shown in the legend in Figure 5, are associated with cases  $A$ ,  $B$ , and  $C$  respectively. It can be seen from Figure 5 that the average values of each strain

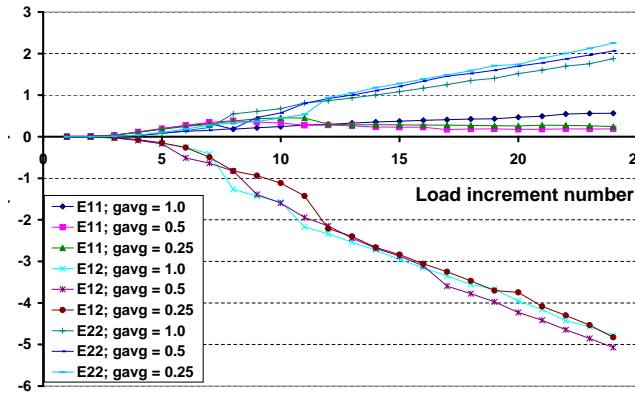


**Figure 5.** Evolution of average strain components for three Delaunay mesh simulations. For each strain component there are curves corresponding to coarse, intermediate, and fine mesh densities.

component are remarkably similar irrespective of the mesh density. It is observed as well that the values of the strain components,  $\bar{\epsilon}_{11}$ , parallel to the direction of the shear sliding cracks are all relatively small. If this component is neglected, a measure of the effective dilation angle  $\psi$  in the control volume can be defined to be

$$\tan \psi \sim -\frac{\bar{\epsilon}_{22}}{2\bar{\epsilon}_{12}}. \quad (14)$$

The effective dilation angle  $\psi$  is plotted in Figure 6 for each mesh density case *A*, *B*, and *C*. It can be seen that as the shear fracture mechanism develops, the dilation angle for each mesh density tends asymptotically to similar constant values ranging approximately between 11 and 13 degrees. It is also observed in Figure 4 that the total length of the random mesh that is activated increases progressively as the mesh density is increased. The cumulative activated length, scaled by the bridge length  $R$  between points *B* and *C* in Figure 1 is plotted in Figure 7. This suggests that the plastic deformation developed in the fracture zone becomes increasingly “smeared” over increasing numbers of cracks as the underlying

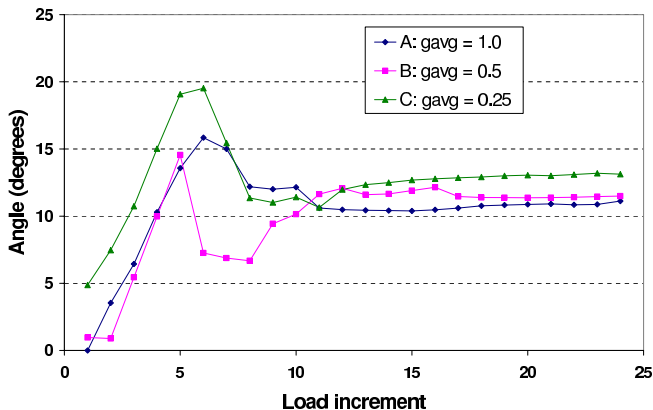


**Figure 6.** Cumulative dilation angle for three Delaunay mesh densities.

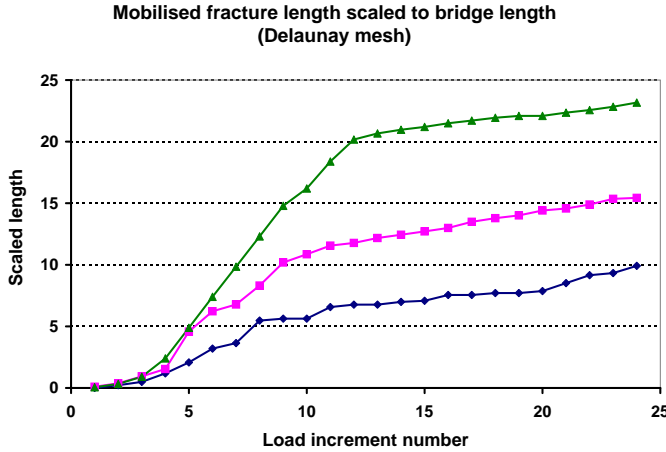


**Figure 7.** Cumulative fracture length scaled to bridge length for three Delaunay mesh densities. Curves are coded as in Figure 6.

mesh becomes finer. The cohesion loss in each mobilized segment will not necessarily be distributed uniformly. It is not clear at present whether this trend would persist if an even finer mesh were to be used. The current results suggest that the cumulative activated length is approximately proportional to the mesh density parameter,  $\rho$ , defined by Equation (12).

**4. Topological characteristics of the tessellation mesh**

The intrinsic connectivity of the mesh structure can play a significant role in determining the simulated fracture pattern. In order to investigate this, two additional numerical simulations (labeled *D* and *E*) were carried out using different intrinsic mesh connectivity properties. For case *D*, the mesh was constructed by subdividing each triangle of an existing Delaunay mesh as illustrated in Figure 8. The result is termed a *split* Delaunay mesh. It can be seen from the figure that the additional mesh segments will have the effect of doubling the number of segments connected to preexisting vertices *D1*, *D2*, *D3*, and *D4*. Additional vertices of the types labeled *C1* and *C2* in Figure 8 are also introduced. The representative vertex *C1* has six segment connections, and representative vertex *C2* has four.

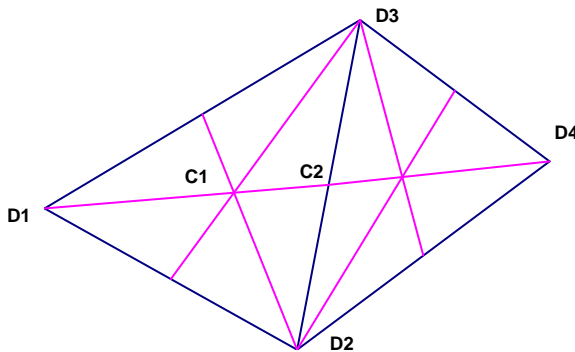


**Figure 8.** Additional mesh segments introduced into two adjacent Delaunay triangles to create a split Delaunay mesh structure.

A second mesh variation, Case *E*, was considered, where the mesh is generated as a classical Voronoi structure. Cases *D* and *E* were compared to case *C*, which corresponds to the finest scale Delaunay mesh discussed in the previous section. Table 2 summarizes the relative frequency of the number of segments joining each internal vertex (junction coordination number) of the meshes used in cases *C*, *D*, and *E*. It can be seen that case *C* (Delaunay mesh) and case *E* (Voronoi mesh) have a most frequent segment coordination number of 6 and 3 connections respectively. Case *D* (split Delaunay) is more complex, showing a mixture of doubled vertex coordinations derived from the parent mesh and new vertices with coordination numbers of 6 and 4 corresponding to the points *C1* and *C2* in Figure 8. A significant proportion of the vertices in case *D* have coordination numbers of 10, 12, and 14. A complete summary of the average mesh segment sizes,  $\bar{g}$ , total segment length,  $L$ , and mesh area,  $A_T$ , for all cases *A* to *E* is given in Table 3.

Coordination number	Relative frequency		
	<i>C</i> (Delaunay)	<i>D</i> (split Delaunay)	<i>E</i> (Voronoi)
3	0	0	0.8436
4	0.0116	0.5000	0.1416
5	0.2474	0	0.0148
6	0.5090	0.3350	0
7	0.2010	0	0
8	0.0296	0.0049	0
9	0.0013	0	0
10	0	0.0416	0
11	0	0	0
12	0	0.0733	0
13	0	0	0
14	0	0.0428	0
15	0	0	0
16	0	0.0024	0

**Table 2.** Mesh junction coordination frequencies for random mesh cases *C*, *D*, and *E*.

Mesh type	Mesh area, $A_T$	Grid size, $\bar{g}$	Mesh length, $L$	Density $\rho = L/\sqrt{A_T}$	Coordination $\lambda = \bar{g}L/A_T$
Delaunay ( <i>A</i> )	160	1.023	547.6	43.3	3.50
Delaunay ( <i>B</i> )	160	0.525	1101.9	87.1	3.61
Delaunay ( <i>C</i> )	72	0.254	1029.9	121.4	3.63
Split Delaunay ( <i>D</i> )	160	0.465	1602.1	126.7	4.66
Voronoi ( <i>E</i> )	160	0.333	663.2	52.4	1.38

**Table 3.** Characteristic mesh parameters.

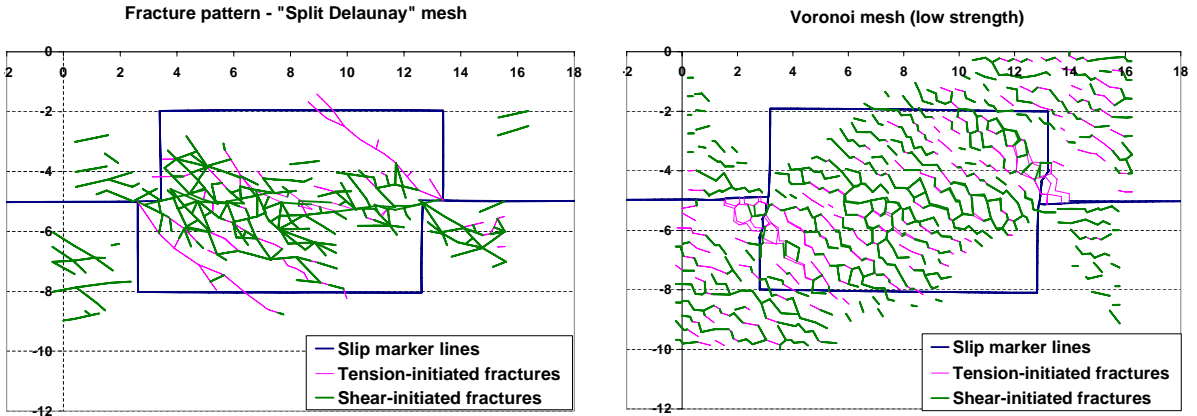


**Figure 9.** Fracture patterns resulting from two different mesh segment junction coordination models. Left: split Delaunay mesh; right, Voronoi mesh.

The loading experiments for cases *D* and *E* were repeated with the same orientation and number of load increments used in cases *A*, *B*, and *C*. The material properties for case *D* were chosen to be the same as those given in Table 1. However, in case *E* the cohesion value of 20 MPa and the tensile strength of 8 MPa, given in Table 1, were reduced to 10 MPa and 4 MPa, respectively, to ensure that a shear band mechanism was fully developed in the bridge region. The fracture patterns developed for the split Delaunay and the Voronoi tessellation runs, *D* and *E*, are shown in Figure 9. A fixed marker region around the rock bridge is included to indicate the general deformation pattern. The zone of fracture activation can be seen to be more concentrated for the split Delaunay mesh than for the Voronoi mesh. The mobilized fragments in case *D* appear to be more angular in character than the rounded grains corresponding to the Voronoi mesh for case *E*. The effective dilation angles corresponding to the simulations *D* and *E* are compared to case *C* in Figure 10. It can be seen that the mesh coordination

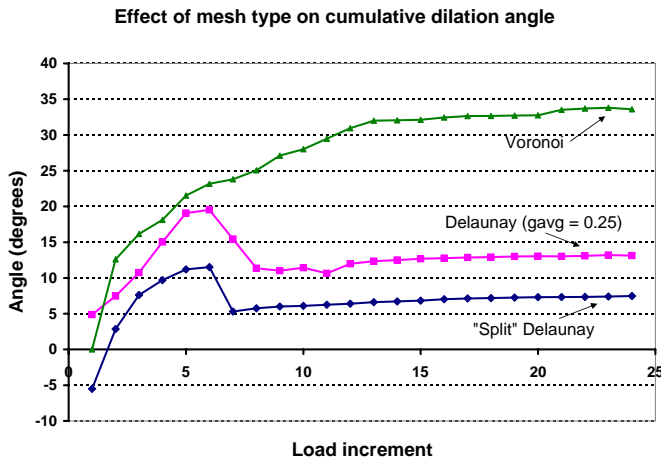


**Figure 10.** Effect of mesh segment coordination on the effective dilation angle for numerical experiments with three distinct meshes.

structure plays a very significant role in determining the effective response of the bridge region. In particular, it is clear that as the average number of segments attached to each mesh junction decreases, the effective dilation angle increases. An equivalent macro model of the rock bridge deformation must therefore include the intrinsic dilation behavior associated with the properties of the micro mesh structure. A simple equivalent macro model for the rock bridge is to assume that it is represented by a single slip discontinuity line joining points  $B$  and  $C$  in Figure 1. In this case the asymptotic behavior of the macro model is determined by defining the following macro properties for the slip line in terms of the micro residual friction angle  $\phi_f$  and the observed dilation angle  $\psi$ . Specifically,

$$\phi_{\text{macro}} = \psi + \phi_f, \quad (15)$$

$$\mu_f^{\text{macro}} = \tan(\psi + \phi_f). \quad (16)$$

Using the residual macroscopic friction coefficient given by Equation (16) and applying the dilation angles  $\psi = 7^\circ$  and  $\psi = 33^\circ$  implied by the asymptotic behavior of Figure 10 yields the equivalent average strain component evolution profiles shown in Figure 11. The plots there show that the macro slip line model is asymptotically equivalent to the corresponding average strain behavior of the underlying micro models after a significant numbers of load increments when the shear band mechanism is fully established. The main problem in applying the equivalent macro model is that it is unclear how the dilation angles of  $\psi = 7^\circ$  and  $\psi = 33^\circ$  can be deduced a priori from the intrinsic mesh structure.

It may be noted by examining the mesh properties reported in Table 3 that an intrinsic relationship can be established between the mean segment size,  $\bar{g}$ , the total length of the mesh segments,  $L$ , and the area of the tessellation mesh,  $A_T$ . Specifically, consider the dimensionless mesh coordination parameter,  $\lambda$ , defined by

$$\lambda = \bar{g}L/A_T. \quad (17)$$

The inferred values of  $\lambda$  are given in the last column of Table 3. It is interesting to note that in the case of the Delaunay mesh (cases  $A$ ,  $B$ , and  $C$ ), the values of  $\lambda$  are very similar ( $\sim 3.6$ ) irrespective of the mesh density,  $\rho$ . However,  $\lambda$  is distinctly different for the split Delaunay and Voronoi mesh cases  $D$  and  $E$  respectively. It appears that  $\lambda$  provides a relative measure of the intrinsic mesh coordination

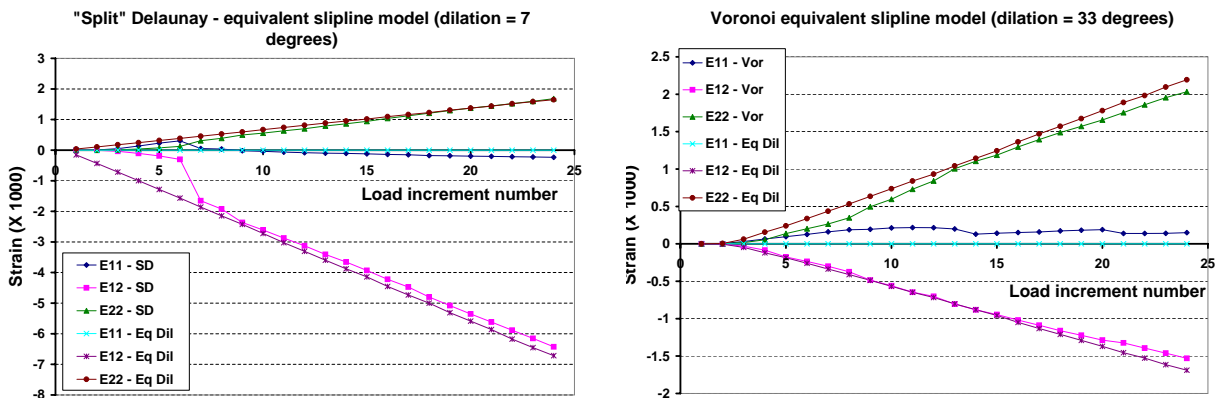


**Figure 11.** Equivalent slip line model asymptotic evolution of average strain in rock bridge region. Left: split Delaunay mesh; right, Voronoi mesh.

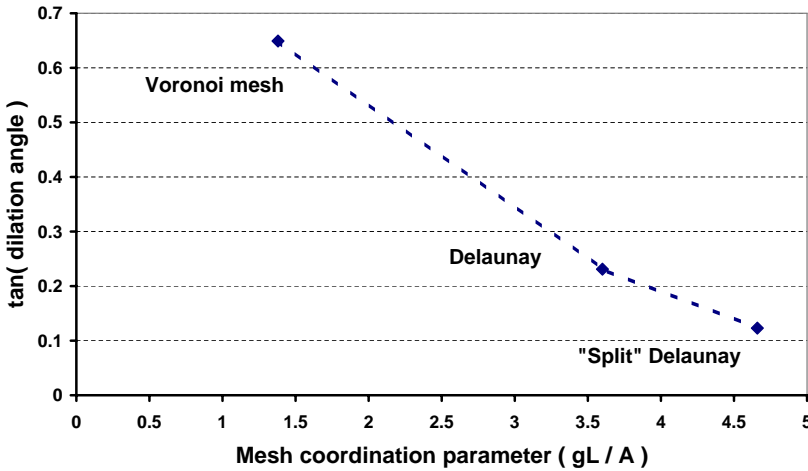


**Figure 12.** Effect of mesh coordination parameter on tangent of effective dilation angle.

topology that is essentially different from the mesh density,  $\rho$ . Figure 12 is a plot of the values of  $\tan \psi$ , inferred from Figure 9, against the coordination parameter  $\lambda$ . (Asymptotic values of  $\psi$  are inferred from Figure 9 to be equal to  $13^\circ$ ,  $7^\circ$ , and  $33^\circ$  for cases *C*, *D*, and *E* respectively). Figure 12 suggests that it may, in fact, be possible to infer the appropriate macro dilation angle  $\psi$  from the intrinsic mesh coordination characteristics summarized by the dimensionless mesh coordination parameter  $\lambda$ . However, a more significant goal is to determine, eventually, whether  $\lambda$  can be determined by direct experimental observation of the actual microscopic fabric structures in rock specimens.

## 5. Conclusions

Numerical experiments have been carried out to determine the effect of a simulated micro structure on equivalent macro shear properties for a simple shear loading experiment relating to the failure of a rock bridge between two preexisting discontinuities. The study addresses only a single micro-to-macro hierarchical step change. It appears that the use of slip and tension-weakening failure parameters in the micro crack model does ensure that the observed macro average strain component evolution is substantially independent of the microscopic mesh density. Less satisfying is the observation of the extent of mesh mobilization associated with different mesh densities which appears to be dependent on the mesh density.

Interestingly, it is found that the intrinsic mesh coordination structure plays an essential role in determining the macro dilation properties of the failed region. This implies that, depending on the nature of a given lattice computational model, equivalent macro behavior (such as may be observed from the averaged results of a laboratory test) may or may not be able to be matched to observed physical behavior. In addition, it appears that some interpretation of the physical equivalent of the mesh junction coordination is required as an additional material parameter that may need to be measured to describe material fabric characteristics. This clearly warrants further investigation in cases of more general three dimensional failure.

The numerical experiments suggest, as well, that a simple dimensionless mesh coordination parameter could provide a useful measure of the effective intrinsic dilation behavior that may be expected to emerge from a selected random mesh crack model. Further studies are required to determine whether this proposed parameter grouping can be extended to a wider variety of computational lattice models.

### Acknowledgements

I thank Professor Arcady Dyskin for inviting me to present an earlier portion of this study at the eighth United States National Conference on Computational Mechanics held in Austin, Texas in 2005. I wish to acknowledge as well a number of helpful comments by the referees.

### References

- [Allodi et al. 2003] A. Allodi, M. Castelli, S. Marelli, and C. Scavia, "Shear band propagation in soft rocks: numerical simulation of experimental results", pp. 23–28 in *ISRM 2003 proceedings - technology roadmap for rock mechanics*, South African Institute of Mining and Metallurgy, 2003.
- [Bobet and Einstein 1998] A. Bobet and H. H. Einstein, "Fracture coalescence in rock-type materials under uniaxial and biaxial compression", *Int. J. Rock. Mech. Min.* **35** (1998), 863–888.
- [Bolander et al. 1996] J. E. Bolander, T. Shirashi, and Y. Isogawa, "An adaptive procedure for fracture simulation in extensive lattice networks", *Eng. Fract. Mech.* **54** (1996), 325–334.
- [Budhu et al. 1999] M. Budhu, S. Ramakrishnan, and G. Frantziskonis, "A lattice type model for particulate media", *Int. J. Numer. Anal. Meth. Geomech.* **23** (1999), 647–671.
- [Chiaia et al. 1997] B. Chiaia, A. Vervuurt, and J. G. M. Van Mier, "Lattice model evaluation of progressive failure in disordered particle composites", *Eng. Fract. Mech.* **57** (1997), 301–318.
- [Crouch and Starfield 1983] S. L. Crouch and A. M. Starfield, *Boundary element methods in solid mechanics*, George Allen & Unwin, London, 1983.
- [Cundall 1988] P. A. Cundall, "Formulation of a three-dimensional distinct element model – Part I. A scheme to detect and represent contacts in a system composed of many polyhedral blocks", *Int. J. Rock. Mech. Min.* **25** (1988), 107–116.
- [Hart et al. 1988] R. Hart, P. A. Cundall, and J. Lemos, "Formulation of a three-dimensional distinct element model – Part II. Mechanical calculations for motion and interaction of a system composed of many polyhedral blocks", *Int. J. Rock. Mech. Min.* **25** (1988), 117–125.
- [Jefferson et al. 2002] G. Jefferson, G. K. Haritos, and R. M. McMeeking, "The elastic response of a cohesive aggregate – a discrete element model with coupled particle interaction", *J. Mech. Phys. Solids* **50** (2002), 2539–2575.
- [Jing 2003] L. Jing, "A review of techniques advances and outstanding issues in numerical modelling for rock mechanics and rock engineering", *Int. J. Rock. Mech. Min.* **40** (2003), 283–353.
- [Kuhn 2005] M. R. Kuhn, "Are granular materials simple? An experimental study of strain gradient effects and localization", *Mech. Mater.* **37** (2005), 607–627.
- [Linkov and Mogilevskaya 1994] A. M. Linkov and S. G. Mogilevskaya, "Complex hypersingular integrals and integral equations in plane elasticity", *Acta Mech.* **105** (1994), 189–205.
- [Lockner and Madden 1991a] D. A. Lockner and T. R. Madden, "A multiple-crack model of brittle fracture 1. Non-time-dependent simulations", *J. Geophys. Res.* **96**:B12 (1991), 19623–19642.
- [Lockner and Madden 1991b] D. A. Lockner and T. R. Madden, "A multiple-crack model of brittle fracture 2. Time-dependent simulations", *J. Geophys. Res.* **96**:B12 (1991), 19643–19654.
- [Mogilevskaya 2000] S. G. Mogilevskaya, "Complex hypersingular integral equation for the piece-wise homogeneous half-plane with cracks", *Int. J. Fract.* **102** (2000), 177–204.
- [Morgan 1999] J. K. Morgan, "Numerical simulations of granular shear zones using the distinct element method - 2. Effects of particle size distribution and interparticle friction on mechanical behavior", *J. Geophys. Res.* **104**:B2 (1999), 2721–2732.

- [Morgan and Boettcher 1999] J. K. Morgan and M. S. Boettcher, "Numerical simulations of granular shear zones using the distinct element method - 1. Shear zone kinematics and micromechanics of localization", *J. Geophys. Res.* **104**:B2 (1999), 2703–2719.
- [Napier and Hildyard 1992] J. A. L. Napier and M. W. Hildyard, "Simulation of fracture growth around openings in highly stressed, brittle rock", *J. S. Afr. Inst. Min. Metall.* **92** (1992), 159–168.
- [Napier and Malan 1997] J. A. L. Napier and D. F. Malan, "A viscoplastic discontinuum model of time-dependent fracture and seismicity effects in brittle rock", *Int. J. Rock. Mech. Min.* **34** (1997), 1075–1089.
- [Napier and Peirce 1995] J. A. L. Napier and A. P. Peirce, "Simulation of extensive fracture formation and interaction in brittle materials", pp. 63–74 in *Proceedings of the second international conference on the mechanics of jointed and faulted rock*, edited by H. P. Rossmanith, Balkema, Rotterdam, 1995.
- [Palmer and Rice 1973] A. C. Palmer and J. R. Rice, "The growth of slip surfaces in the progressive failure of over-consolidated clay", *Proc. Roy. Soc. Lond. A* **332** (1973), 527–548.
- [Potyondy and Cundall 2004] D. O. Potyondy and P. A. Cundall, "A bonded-particle model for rock", *Int. J. Rock. Mech. Min.* **41** (2004), 1329–1364.
- [Rechenmacher 2006] A. L. Rechenmacher, "Grain-scale processes governing shear band initiation and evolution in sands", *J. Mech. Phys. Solids* **54** (2006), 22–45.
- [Scavia 1992] C. Scavia, "A numerical technique for the analysis of cracks subjected to normal compressive stresses", *Int. J. Numer. Methods Eng.* **33** (1992), 929–942.
- [Sellers and Napier 1997] E. Sellers and J. A. L. Napier, "A comparative investigation of micro-flaw models for the simulation of brittle fracture in rock", *Comput. Mech.* **20** (1997), 164–169.
- [Uenishi and Rice 2003] K. Uenishi and J. R. Rice, "Universal nucleation length for slip-weakening rupture instability under nonuniform fault loading", *J. Geophys. Res.* **108**:B1 (2003), ESE 17–1 – 17–13.

Received 24 Aug 2007. Accepted 10 Dec 2007.

JOHN NAPIER: john.napier@pixie.co.za

School of Computational and Applied Mathematics, University of the Witwatersrand, Johannesburg, South Africa